First Experience of ^{18}F-Alfatide in Lung Cancer Patients Using a New Lyophilized Kit for Rapid Radiofluorination

Weixing Wan*[1,2], Ning Guo*[3–5], Donghui Pan[1], Chunjing Yu[2], Yuan Weng[2], Shineng Luo[1], Hong Ding[1], Yuping Xu[1], Lizhen Wang[1], Lixin Lang[3], Qingguo Xie[4], Min Yang[1], and Xiaoyuan Chen[3]

[1]Key Laboratory of Nuclear Medicine, Ministry of Health, Jiangsu Key Laboratory of Molecular Nuclear Medicine, Jiangsu Institute of Nuclear Medicine, Wuxi, China; [2]Department of Nuclear Medicine, Wuxi No. 4 People's Hospital, Wuxi, China; [3]Laboratory of Molecular Imaging and Nanomedicine, National Institute of Biomedical Imaging and Bioengineering, National Institutes of Health, Bethesda, Maryland; [4]Department of Biomedical Engineering, Huazhong University of Science and Technology, Wuhan, Hubei, China; and [5]Center for Molecular Imaging and Translational Medicine, Xiamen University, Xiamen, Fujian, China

^{18}F-FPPRGD2, which was approved for clinical study recently, has favorable properties for integrin targeting and showed potential for antiangiogenic therapy and early response monitoring. However, the time-consuming multiple-step synthesis may limit its widespread applications in the clinic. In this study, we developed a simple lyophilized kit for labeling PRGD2 peptide (^{18}F-AlF-NOTA-PRGD2, denoted as ^{18}F-alfatide) using a fluoride–aluminum complex that significantly simplified the labeling procedure. **Methods:** Nine patients with a primary diagnosis of lung cancer were examined by both static and dynamic PET imaging with ^{18}F-alfatide, and 1 tuberculosis patient was investigated using both ^{18}F-alfatide and ^{18}F-FDG imaging. Standardized uptake values were measured in tumors and other main organs at 30 min and 1 h after injection. Kinetic parameters were calculated by Logan graphical analysis. Immunohistochemistry and staining intensity quantification were performed to confirm the expression of integrin $\alpha_v\beta_3$. **Results:** Under the optimal conditions, the whole radiosynthesis including purification was accomplished within 20 min with a decay-corrected yield of 42.1% ± 2.0% and radiochemical purity of more than 95%. ^{18}F-alfatide PET imaging identified all tumors, with mean standardized uptake values of 2.90 ± 0.10. Tumor-to-muscle and tumor-to-blood ratios were 5.87 ± 2.02 and 2.71 ± 0.92, respectively. **Conclusion:** ^{18}F-alfatide can be produced with excellent radiochemical yield and purity via a simple, 1-step, lyophilized kit. PET scanning with ^{18}F-alfatide allows specific imaging of $\alpha_v\beta_3$ expression with good contrast in lung cancer patients. This technique might be used for the assessment of angiogenesis and for planning and response evaluation of cancer therapies that would affect angiogenesis status and integrin expression levels.

Key Words: RGD peptide; alfatide; aluminum fluoride; PET; lung cancer

J Nucl Med 2013; 54:691–698
DOI: 10.2967/jnumed.112.113563

Recently, encouraging reports of successful antiangiogenic therapy in combination with chemotherapy and radiotherapy have been demonstrated in various carcinomas and metastatic malignant tumor entities (*1–4*). Consequently, there is an increasing demand for noninvasive imaging to facilitate early response monitoring and screening of the appropriate patients who will benefit from antiangiogenic treatment with positive effects (*5,6*). Integrin $\alpha_v\beta_3$, which plays a key role in the regulation of cellular activation, survival, and migration, is one of the most important members in the integrin family (*7–9*). The ability to visualize and quantify $\alpha_v\beta_3$ integrin expression via specific targeting ligands will provide unique opportunities for evaluating tumor neovascularization. Great efforts have been made in developing radiolabeled integrin-targeting agents (*4,10–13*). Various arginine-glycine-aspartic acid (RGD)–containing peptide probes have been tested, because cyclic RGD peptides have high affinity and selectivity for integrin $\alpha_v\beta_3$. RGD peptides have been radiolabeled and evaluated with ^{18}F (*14*), ^{64}Cu (*15*), ^{68}Ga (*16,17*), ^{76}Br (*13*), and ^{89}Zr (*18*) for integrin $\alpha_v\beta_3$–targeted PET imaging in xenograft models.

^{18}F is a popular radioisotope for labeling peptides because of its well-suited physical half-life (109.7 min) for routine clinical use. Therefore, several ^{18}F-labeled RGD peptide tracers have been tested in oncologic patients, including ^{18}F-galacto-RGD (*4*) and ^{18}F-AH11585 (*19*). Both of these radiotracers are peptides based on monomeric cyclic RGD. With favorable pharmacokinetics and binding affinity for $\alpha_v\beta_3$ integrin, dimeric and multimeric RGD peptides are superior to the monomeric analogs (*10,20*), most likely because of the polyvalency effect. With potential specificity of imaging $\alpha_v\beta_3$ integrin expression in oncology,

Received Sep. 5, 2012; revision accepted Nov. 12, 2012.
For correspondence or reprints contact either of the following: Xiaoyuan Chen, Laboratory of Molecular Imaging and Nanomedicine, NIBIB, National Institutes of Health, 31 Center Dr., 1C22, Bethesda, MD 20892.
E-mail: shawn.chen@nih.gov
Min Yang, Key Laboratory of Nuclear Medicine, Ministry of Health, Jiangsu Institute of Nuclear Medicine, 20 Qian Rong Rd., Wuxi, China 214063.
E-mail: ymzfk@yahoo.com.hk
*Contributed equally to this work.
Published online Apr. 3, 2013.

the dimeric RGD peptide ^{18}F-FPPRGD2 was obtained recently for further evaluation approved by the Food and Drug Administration (*6*).

However, all these ^{18}F-labeled compounds suffer from multistep time-consuming and low-yield synthetic procedures, limiting their widespread use as routine tracers in the clinic. The application of chelation chemistry, which allows the radiotracer to be prepared without the need of high-performance liquid chromatography, has led to the recent development of ^{18}F-fluoride–aluminum complexes to radiolabel peptides. Lang et al. (*21*) successfully prepared ^{18}F-AlF-NOTA-PRGD2 (denoted as ^{18}F-alfatide as shown in Fig. 1), and Guo et al. (*22*) evaluated and compared the pharmacokinetics of this new fast-labeling dimeric RGD compound with other well-developed dimeric RGD peptides in U87MG xenografts. It was shown that ^{18}F-alfatide has promising imaging properties and pharmacokinetics that are comparable, or superior, to those of ^{18}F-FPPRGD2. Thus, it is encouraging that the recently introduced kit formulation method for rapid radiofluorination provides a strategy for simplifying the labeling procedure for RGD peptides and shows potential for facilitating clinical translation. As the next logical step, we are now focusing on specific tumor entities to evaluate the clinical use of ^{18}F-alfatide.

The aim of this study was to develop the kits for the dimeric RGD peptide and prove the feasibility of PET imaging in lung cancer patients with squamous or adenomatous carcinoma using ^{18}F-alfatide. Quantitative analysis and pharmacokinetics studies were also conducted to further analyze the specificity of tracer accumulation.

MATERIALS AND METHODS

Radiopharmaceutical Preparation

NOTA-PRGD2 was synthesized previously (*21*). $AlCl_3 \cdot 6H_2O$ and other chemicals obtained commercially were of analytic grade and used without further purification. No-carrier-added ^{18}F was obtained from an in-house cyclotron (HM-7; Sumitomo Heavy Industries Ltd.). Reversed-phase extraction Sep-Pak C18 cartridges, which were used to purify the radiolabeled peptides, were acquired from Waters. Analytic reversed-phase high-performance liquid chromatography using a Phenomenex C18 column (Luna, 5 μm, 250 × 4.6 mm) was performed on a chromatography system (Waters) with a 2487 Dual λ absorbance detector (Waters) and a Perkin-Elmer radiomatic flow scintillation analyzer. With a flow rate of 1 mL/min, the mobile phase stayed at 95% solvent A (0.1% trifluoroacetic acid in water) and 5% B (0.1% trifluoroacetic acid in acetonitrile [MeCN]) at 0–2 min and was changed to 35% solvent A and 65% solvent B at 32 min.

Stock solutions of NOTA-PRGD2 and $AlCl_3 \cdot 6H_2O$ were dissolved in deionized water. Kits were made with varying amounts of NOTA-PRGD2 (8–32 nmol) and $AlCl_3 \cdot 6H_2O$ (3–12 nmol) stock solutions. The filled vials were frozen and then transferred to the shelf of the Labconco Freeze Dry System cooled to −16°C. When the vacuum went below 13.3 Pa (100 mTorr), the shelf temperature was increased to 0°C. After 16 h, the shelf temperature was increased to 20°C for 4 h. The vials were then sealed under vacuum and removed from the lyophilizer.

The lyophilized peptide was radiolabeled by adding ^{18}F (740–3,700 MBq [20–100 mCi]) in 100–200 μL of deionized water and an equal volume of sodium acetate–acetonitrile buffer solution (pH 2–6) to the crimp-sealed vial and then heating to 70°C –110°C for 5–30 min. After being cooled, the vial contents were diluted with 10 mL of water and loaded onto an activated C18 cartridge. The cartridge was washed again with water (10 mL), and the desired labeled peptide ^{18}F-alfatide was eluted with 10 mM HCl in ethanol (1 mL). The product was reconstituted in saline and passed through a 0.22-μm Millipore filter into a sterile vial for further studies.

The percentage isolated yield in the product vial was determined by measuring the activity found in the Sep-Pak C18 cartridge, reaction vial, water wash, and product vial to account for the total activity. When the isolated yield calculation was compared with the decay-corrected method, the yields were found to be essentially identical, indicating that all the ^{18}F activity was counted.

The purified radiolabeled peptides in saline were stored at 37°C and 4°C. The radiochemical purity of the solution was used to test the labeling yield at different time points (0, 1, 2 and 4 h).

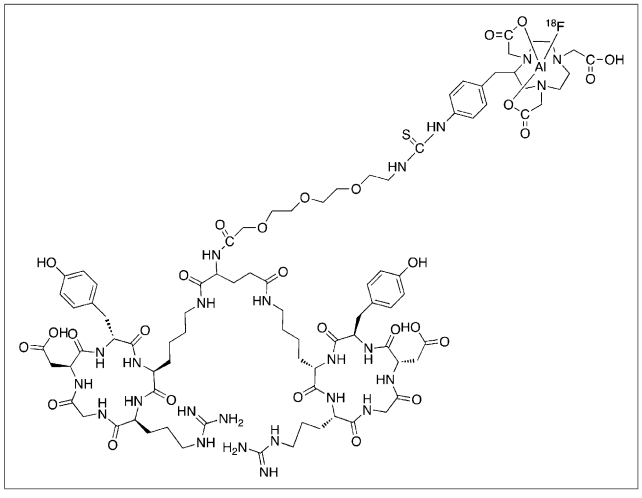

FIGURE 1. Chemical structure of ^{18}F-AlF-NOTA-PRGD2 (^{18}F-alfatide) peptide.

Patients

The study protocol was approved by the ethics committee of Wuxi no. 4 People's Hospital, and each patient gave written and informed consent before the study. Nine male patients (age range, 57–79 y) who suffered from lung cancer were included and examined in this study. Patient selection was focused on lung cancer because there is considerable evidence reported that squamous cancer cells express integrin $\alpha_v\beta_3$. Diagnosis before scanning was made by biopsy, CT, or ^{18}F-FDG PET. After scanning, the diagnosis was confirmed by surgery and histopathologic examination of the resection specimen or by combined analysis of morphologic imaging and the patient's clinical data as well as history. One female patient with tubercular lymph nodes was investigated by comparing ^{18}F-FDG and ^{18}F-alfatide imaging. The patient information is summarized in Table 1.

PET/CT Imaging

PET/CT imaging was performed on a Biograph 64 PET/CT scanner (Siemens) in all instances. ^{18}F-alfatide (224.56 ±

TABLE 1
Patient Characteristics and PET Quantifications

Patient no.	Age (y)	Diagnosis	Modality
1	73	Adenomatous carcinoma in lung right lobe, low-graded	PET/CT immunohistology
2	64	Squamous carcinoma in lung left lobe, stage II	PET/CT immunohistology
3	79	Squamous carcinoma in lung right lobe center of large area, stage III, with blocking inflammation	PET/CT
4	71	Squamous carcinoma in lung right lobe stage II-III, with lymph node and bone metastasis	PET/CT immunohistology
5	57	Squamous carcinoma in lung left lobe, low-graded, with lymph node metastasis	PET/CT
6	67	Squamous carcinoma in lung right lobe, low-graded	PET/CT immunohistology
7	69	Squamous carcinoma in lung left lobe stage III-IV	PET/CT
8	62	Squamous carcinoma in lung right lobe, low-graded, with lymph node metastasis	PET/CT immunohistology
9	48	Squamous carcinoma in lung left lobe stage, low-graded	PET/CT immunohistology
10	26	Whole-body lymph node tuberculosis	PET/CT

38.2 MBq) was injected intravenously in all patients. No specific subject preparation, such as fasting, was requested on the day of imaging. Two imaging protocols were applied to study the whole-body tracer distribution and time–activity curves. In 6 patients, 30- or 60-min (depending on the age and state of illness) dynamic scans were acquired, with the detector rings covering the region of tumor and heart so that the time–activity curves of malignant lesions and arterial blood input functions could be obtained. The dynamic scans were followed by a static scan. A static emission scan was acquired for each subject beginning on average 60 min after injection of ^{18}F-alfatide, covering a field of view from the abdomen to the base of the skull (5–7 bed positions, 5 min per bed position). PET images were reconstructed with 3-dimensional ordered-subset expectation maximization. The frame rates of dynamic scans were 10 × 30, 5 × 60, 5 × 120, and 10 × 240 s. The images were attenuation corrected with the transmission data from CT.

Image Analysis

In biodistribution analysis from static images, regions of interest (ROIs) were placed over the tumor and major organs (heart, lung, liver, spleen, intestine, kidneys, and muscle) with the assistance of corresponding CT images. The results were expressed in standardized uptake value (SUV), which was calculated according to the following formula: (measured activity concentration [Bq/mL] × body weight [g]/injected activity [Bq]). Biodistribution SUV quantification for 30 min after injection was conducted in dynamic image analysis, where only main organs could be covered in 1 bed position. In dynamic PET image analysis, ROIs were measured with the Inveon Research Workplace software (version 3.0; Siemens). ROIs were determined by manually superimposing the ellipsoid volume of interest (VOI) to the target tissue on the last frame of the entire 60-min (or 30-min) dynamic image sequence. Then a threshold of 30% maximum was set to screen the voxels with lower values in the entire VOI because of possible tumor heterogeneity and shape irregularity. The time–activity curves were derived by superimposing the same VOI on each time frame of the entire dynamic image sequence, and the value of each time point represents the overall concentration of radioactivity in the tissue. The activity concentrations, which were converted to SUV, were determined by the mean pixel intensity within each VOI. The arterial blood input function was estimated by drawing a VOI in the region of left ventricle on the reconstructed PET image at 0.5 min (the second frame of dynamic PET image series). The region of muscle was selected as the reference tissue.

Kinetic Modeling and Parameter Estimation

As reported in our previous study, a 2-tissue-compartment (3-compartment) model best characterized the tumor and other specific binding processes of RGD peptide (*22,23*). Therefore, a 1-tissue-compartment (2-compartment) model where the third compartment (specific binding) is not suitable to be described was used for muscle as a reference tissue. The 3-compartment model consists of unmetabolized radiotracer in arterial blood plasma (C_p), free or nonspecific binding tracer in interstitial and intracellular space (C_t), and tracer bound specifically to integrin (C_m). Both C_t and C_m occupy the same physical volume. The *ROI(t)* represents the sum of radioactivity from all compartments and includes the plasma volume fraction. Similarly, the 2-compartment model describes RGD tracer kinetics using muscle as reference tissue, and *ref(t)* represents free (nonspecific binding) tracer in the reference tissue (muscle) region. Generally speaking, kinetic parameters K_1 (mL/g/min), k_2 (1/min), k_3 (1/min), and k_4 (1/min) represent the transport or binding rates of plasma perfusion into tissue, clearance from plasma, specific binding, and dissociation, respectively.

On the basis of the Logan plot shown in Equation 1 (*24,25*), the ratio between the integral of $C_p(t)$ and the instantaneous value of *ROI(t)* and the ratio between the integral and the instantaneous value of *ROI(t)* become linearly related when the exchange between the target tissue and plasma reaches an equilibrium ($t > t^*$).

$$\frac{\int_0^T ROI(t)dt}{ROI(T)} = DV\frac{\int_0^T C_p(t)dt}{ROI(T)} + Int \quad (t>t*). \qquad \text{(Eq. 1)}$$

DV denotes the volume of distribution (V_T) and can be easily calculated from the linear regression. *DV* is a measure of the capacity of tissue to bind a particular tracer and can be regarded as the sum of specific (V_S) and nonspecific distribution (V_{ND}). Total V_T is defined in Equation 2 (*26*).

$$V_T = V_S + V_{ND} = \frac{K_1}{k_2}\left(1 + \frac{k_3}{k_4}\right). \quad \text{(Eq. 2)}$$

In the original Logan plot estimation, an arterial blood input function is required. Unfortunately, blood sampling faces technical challenges and brings radiation exposure to researchers. A reformulation of the Logan analysis, which uses a reference region, provides the possibility to estimate the kinetic parameters without arterial blood sampling (*27*). We selected muscle as the reference tissue because of its negligible integrin expression. The relationship between muscle and plasma is expressed in Equation 3.

$$\frac{\int_0^T ref(t)dt}{ref(T)} = DV^{ref}\frac{\int_0^T C_p(t)dt}{ref(T)} + \frac{1}{k_2^{ref}}. \quad \text{(Eq. 3)}$$

DV^{ref} and k_2^{ref} are the parameters volume of distribution and k_2 of reference tissue.

Thus, the normalized integral of activity in the tumor versus the normalized integral of activity in the muscle becomes linear according to Equation 4:

$$\frac{\int_0^T ROI(t)dt}{ROI(T)} = DVR\left(\frac{\int_0^T ref(t)dt + ref(t)/k_2^{ref}}{ROI(T)}\right) + Int'. \quad \text{(Eq. 4)}$$

The ratio of integrated tumor uptake and tumor uptake was set as the *y*-axis. The ratio of integrated reference tissue uptake and tumor uptake was set as the *x*-axis in the Logan plot. The slope of the linear portion of the Logan plot is distribution volume ratio (*DVR*). Binding potential ($Bp_{ND} = k_3/k_4$), a macroparameter reflecting the binding affinity in vivo, could be derived from *DVR* ($Bp_{ND} = DVR - 1$).

Tissue Samples and Immunohistochemistry Collection

For immunohistochemistry, sampled specimens were snap-frozen in liquid nitrogen and stored at −70°C until staining was performed. Tissue samples were taken within 1 wk after scanning from the tumor regions with the maximum tracer uptake and, when possible, from regions with low tracer uptake. Frozen tumor tissues were sectioned and stained using the biotinylated monoclonal anti-$\alpha_v\beta_3$ antibody. Sections were processed by peroxidase staining. Light microscopic evaluation of the density of $\alpha_v\beta_3$-positive tissue was performed. Briefly, areas with the highest density of $\alpha_v\beta_3$-positive tissue were identified using scanning magnification. Subsequently, $\alpha_v\beta_3$-positive areas were counted in 5 adjacent microscopic fields using a ×40 objective lens and a ×10 ocular lens, corresponding to an area of 0.588 mm^2. Microvessel density and staining intensity were determined by a senior pathologist, who was masked to the results of the corresponding SUV.

Statistical Analysis

SUV and quantitative kinetic parameters determined from PET data were expressed as mean ± SD.

RESULTS

Kit Optimization

The kit consists of NOTA-PRGD2 and $AlCl_3$, and the amounts were optimized. We found that the reaction was most efficient at an amount of 16 nmol for NOTA-PRGD2. Using the kit prepared with the optimal amounts of NOTA-PRGD2 peptide and $AlCl_3$, we conducted additional studies to assess the necessary reaction temperature, pH of buffer solution, and timing for the labeling procedure and how the ^{18}F activity would affect labeling yields (shown in the supplemental data; supplemental materials are available online only at http://jnm.snmjournals.org). These studies showed that labeling yield was improved as the temperature increased, with maximum yields peaking at 100°C or more. The optimal pH value for labeling ranges from 2 to 4. Heating for 10 min provided high yields, with longer time possibly enhancing the yields slightly but not enough to warrant the loss in isotopic decay that would otherwise occur. Naturally, the labeling yield stayed consistent when the amount of ^{18}F was 740–2,590 MBq (20–70 mCi). The labeling yield was significantly decreased when more ^{18}F activity was added. Under the optimal condition, the whole radiosynthesis, including purification was accomplished within 20 min, with a decay-corrected yield of 42.1% ± 2.0% and radiochemical purity of more than 95%. The specific activity of ^{18}F-alfatide was calculated to be at least 37 GBq (1,000 mCi)/μmol.

Biodistribution

Figure 2 shows the distribution of ^{18}F-alfatide at 1 h after intravenous administration in a representative lung cancer patient. Major organs with relatively high uptake were labeled in a maximum-intensity-projection PET image (Fig. 2A). The corresponding coronal PET/CT fusion image showed the tracer distribution in the main area of body including tumor (Fig. 2B). The transaxial PET/CT and CT images focusing on tumors are also shown in Figure 2C. The tumor area with tracer uptake showed intense staining of integrin in the neovasculature (Fig. 2D). The results of the SUV measurements for tumors and other main organs are summarized in Table 2. The mean SUVs were 2.90 ± 0.10 for tumor, 1.07 ± 0.07 for blood, and 0.49 ± 0.04 for muscle at 1 h after injection. The 1-h tumor-to-blood and tumor-to-muscle ratios were calculated to be 2.71 ± 0.92 and 5.87 ± 2.02, respectively. Integrin $\alpha_v\beta_3$ expression could be confirmed by immunohistochemistry in all primary tumor specimens. The highest activity accumulation was found in the kidneys and bladder, demonstrating renal clearance. The liver, spleen, and intestines also showed moderate uptake. Minimal radiotracer accumulation was found in the brain ventricles and thyroid gland.

Patient Study

All tumors could be clearly identified by ^{18}F-alfatide. ^{18}F-alfatide PET identified 2 patients' lymph node metastatic lesions, which were confirmed by corresponding

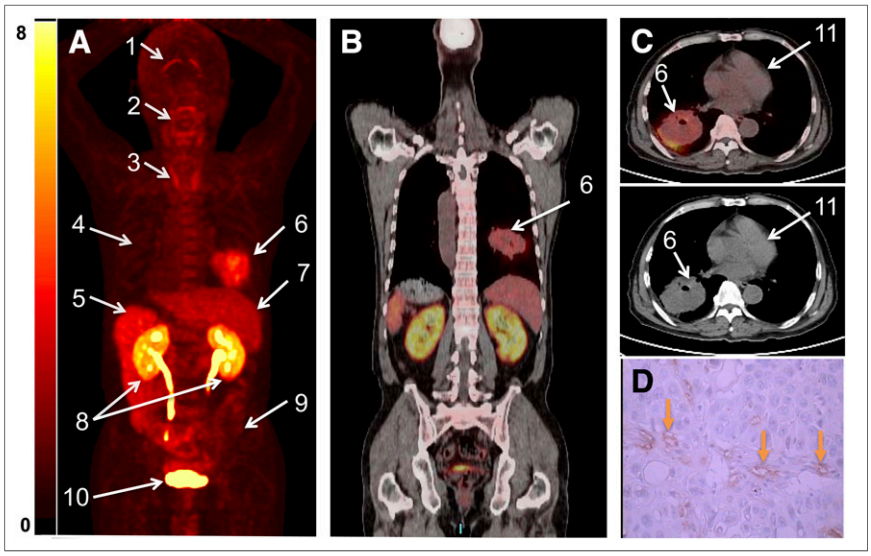

FIGURE 2. (A) Representative coronal maximum-intensity-projection PET image shows distribution of ^{18}F-alfatide (SUV) at 1 h after injection in lung cancer patient (patient 6 in Table 1). Major organs and regions are labeled with arrows brain ventricles (*1*), salivary–oropharyngeal cavity (*2*), thyroid gland (*3*), lungs (*4*), spleen (*5*), tumor (*6*), liver (*7*), kidneys (*8*), intestine (*9*), bladder (*10*), and heart (*11*). (B) Corresponding PET/CT fusion image at certain coronal slice further shows uptake of tumor and other organs. (C) Corresponding transaxial PET/CT fusion image (upper) and CT image (middle). (D) Intense staining of neovasculature without staining of tumor cell.

^{18}F-FDG scans (Fig. 3). Some small metastatic lesions in the bone could also be detected in ^{18}F-alfatide imaging (tumor-to-bone ratio, ~1.7) (Fig. 4). A 26-y-old female patient underwent both ^{18}F-FDG and ^{18}F-alfatide static PET/CT scans within 3 d. Despite obvious ^{18}F-FDG uptake in the mesenteric lymph nodes, ^{18}F-alfatide appeared to be negative in this scrofula patient (Fig. 5). Although ^{18}F-FDG PET remains superior for tumor detection and staging in lung cancer, ^{18}F-alfatide PET imaging may provide additional information for screening tumor-induced inflammation and scrofula lesions.

Immunohistochemistry

As shown in Figure 6, immunohistochemistry results confirmed integrin $\alpha_v\beta_3$ expression in primary tumors. Integrin $\alpha_v\beta_3$ expression in addition to staining of the neovasculature could be seen on the tumor cells. Rarely, integrin $\alpha_v\beta_3$ could be observed in normal tissue. Unfortunately, no sample was collected from the 2 patients with lymph node metastasis. The integrin expression level and microvessel density were quantified and summarized in Figure 6B. In Figure 6B, according to the RGD uptake, the samples were grouped as high and moderate, and the corresponding integrated optical densities were 30,459.36 ± 2,298.71 (n = 4) and 26,748.64 ± 2,226.64 (n = 3). As a control, the normal tissue showed a minimal integrated optical density of 567.75 ± 88.63 (n = 5).

Time–Activity Curves and Kinetic Quantification

In all dynamic scans, tumors showed rapid tracer accumulation during the first 10 min and reached a plateau with only a minimal decrease of uptake though the entire 60-min time course (Fig. 7A). Other normal organs such as the liver and heart showed a peak at early time points (<1 min) because of blood perfusion with high concentration of radioactivity. The uptake in these regions dropped rapidly afterward, which is consistent with a previous report (*28*). The arterial blood input function was estimated by drawing a VOI in the region of the left ventricle on reconstructed PET/CT images at 0.5 min (the second frame of the dynamic PET image series). The method permits the extraction of the input function from the left ventricle while keeping the peak of tracer concentration in blood with good accuracy. A region of muscle was selected as the reference tissue (the region with almost the same blood input function but without specific binding). The corresponding time courses were shown in Figure 7A. Kinetic parameters were summarized in Figure 7B. The binding potential in the tumor was 3.63 ± 1.28; V_Ts were 1.55 ± 0.07 for the tumor and 0.35 ± 0.15, 1.52 ± 0.28, and 0.27 ± 0.05, respectively, for healthy lung, liver, and muscle. Compared with the other

TABLE 2
SUVs Normalized to Weight for Various Organs

Organ	Hours after administration of ^{18}F-alfatide	
	0.5	1
Tumor	2.91 ± 0.73	2.90 ± 0.10
Liver	3.02 ± 0.54	2.74 ± 0.58
Thyroid gland	1.69 ± 0.44	2.04 ± 0.35
Spleen	4.00 ± 0.60	3.70 ± 0.60
Kidneys	7.14 ± 0.96	5.55 ± 0.75
Muscle	0.55 ± 0.15	0.49 ± 0.04
Heart	1.57 ± 0.27	1.07 ± 0.07
Lung	0.45 ± 0.11	0.26 ± 0.06
Bone	1.73 ± 0.45	1.67 ± 0.68
Intestine	—	2.15 ± 0.28
Bladder	—	69.32 ± 58.28
Brain	—	0.09 ± 0.04
Brain ventricles	—	1.69 ± 0.04
Tumor-to-muscle ratio	5.70 ± 2.24	5.87 ± 2.02
Tumor-to-blood ratio	1.87 ± 0.49	2.71 ± 0.92

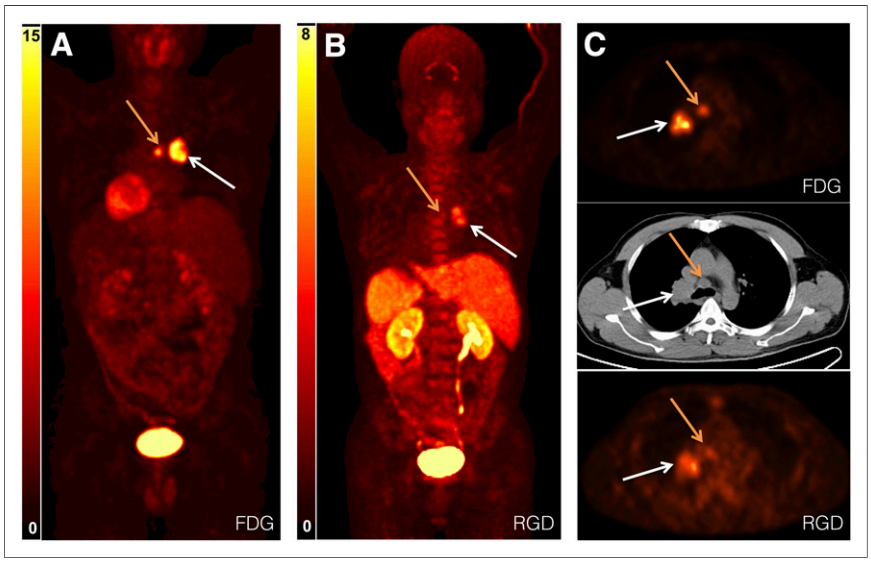

FIGURE 3. ^{18}F-FDG (A) and ^{18}F-alfatide (B) maximum-intensity-projection imaging of patient (patient 8 in Table 1) with primary squamous carcinoma (white arrow) and lymph node metastasis (yellow arrow). (C) Transaxial PET image with administration of ^{18}F-FDG (upper) and ^{18}F-alfatide (lower) and corresponding CT image (middle) covering carcinoma and lymph node metastasis.

normal tissue, the V_Ts in the tumor represent specific accumulation in this region.

DISCUSSION

Noninvasive PET imaging of integrin $\alpha_v\beta_3$ has become an important tool for tumor diagnosis and treatment monitoring in both preclinical and clinical studies (*4,29–31*). Currently, several ^{18}F-labeled RGD peptides have been evaluated in clinical trials, and a more widespread use of PET imaging of integrin expression is expected in the near future. ^{18}F-FPPRGD2 is one of the promising radiolabeled RGD peptides, with desirable pharmacokinetic properties for clinical noninvasive PET imaging of $\alpha_v\beta_3$ expression. It shows high binding affinity to integrins and favorable pharmacokinetics, with quick renal clearance in the body. However, the time-consuming multiple-step synthetic procedure required for ^{18}F-FPPRGD2 preparation may hinder the widespread use of this ^{18}F-labeled RGD tracer. The rather complex synthesis of other RGD peptides being tested in the clinic, for example, ^{18}F-galacto-RGD, also hampers its broad use in large clinical studies (*4*). We developed a simple lyophilized kit for ^{18}F labeling with RGD peptide, which would provide a useful platform for commercial development.

The kit and formulation were optimized with regard to reaction temperature, pH value of the buffer, reaction time, and ^{18}F activity (supplemental data). These studies confirmed the excellent labeling yield under the optimal conditions, which was higher than previously reported (5%–25%) (*21*). Our experience showed that the alfatide-labeling method is reliable, giving similar labeling yields from day to day. And after more than 100 kit labels, we haven't encountered even a single failure. By formulating peptides into kits, uncertainties about obtaining a successful labeled product can be avoided. Because of the simplicity of the method, an advantage is that additional studies can be easily performed in a single day. Radiochemical stabilities of radiopharmaceuticals stored over extended periods, including self-radiolysis, are critical to their safe, effective use in the diagnosis and treatment of disease. Only minor changes were observed in the radiochemical composition of up to 4 h (with 1.8% radiochemical decomposition). This rate of change was acceptable for clinical ^{18}F-labeling preparations over this period and suitable for in vivo use for at least 4 h after the preparation.

In this study, we successfully showed the feasibility of PET imaging of $\alpha_v\beta_3$ expression in lung squamous carcinoma and adenomatous carcinoma patients with good contrast using ^{18}F-AlF-NOTA-PRGD2 (^{18}F-alfatide). To the best of our knowledge, this is the first time that this 1-step synthesized ^{18}F-labeled RGD peptide was applied to the clinic for noninvasive determination of $\alpha_v\beta_3$ expression. No adverse events were found in the first human subject during the pilot study. The biodistribution showed low

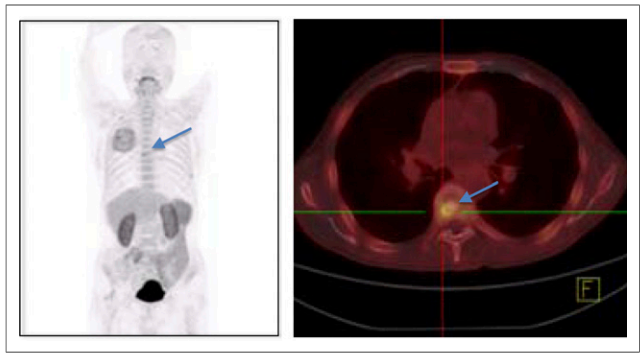

FIGURE 4. ^{18}F-alfatide PET and corresponding PET/CT image of lung cancer patient with bone metastasis (patient 4 in Table 1). (Left) Maximum-intensity-projection whole-body PET image. (Right) Transaxial PET/CT image covering bone metastatic lesion, 1 h after injection of ^{18}F-alfatide. Arrows point to bone metastatic lesion.

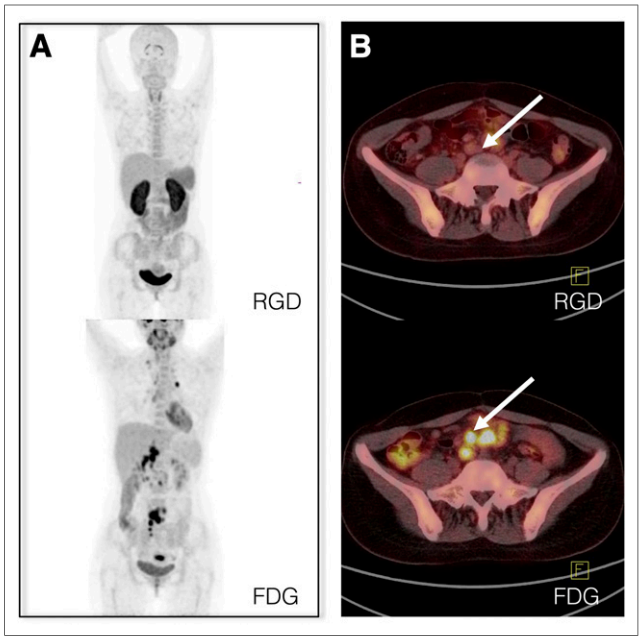

FIGURE 5. ^{18}F-alfatide and corresponding ^{18}F-FDG PET/CT scans of scrofula patient (patient 10 in Table 1). (A) Maximum-intensity-projection PET images of scrofula patient at 1 h after injection of ^{18}F-alfatide (upper) and ^{18}FDG (lower). (B) Transaxial PET/CT fusion image covering intestine. Negative uptake at 1 h after injection of ^{18}F-alfatide (upper) and high uptake in scrofula patient at 1 h after injection of ^{18}F-FDG (lower) are shown. Arrows point to tubercular lymph nodes.

tracer uptake in background (lung) and muscle, with high tumor-to-background ratios, resulting in desirable image contrast and clear identification of most primary tumors and metastatic lesions. The tumor-to-blood and tumor-to-muscle ratios of ^{18}F-alfatide in lung cancer were consistent with the corresponding value of ^{18}F-galacto-RGD (*32*) in head and neck tumors and higher than the corresponding value of ^{99m}Tc-3PRGD2 (*33*) in lung cancers. The relatively low background in specific tissues and organs such as the lungs and breast may allow clear diagnosis and evaluation of tumors present in these areas. Clear background in the brain will also fulfill brain tumor or metastatic lesion detection because the existence of tumors will result in broken blood–brain barrier (*31*).

Dynamic PET scans and kinetic modeling were performed to further analyze the pharmacokinetics of ^{18}F-alfatide, which shows favorable pharmacokinetic parameters with high binding potential, demonstrating desirable binding affinity to integrin expression in vivo. The V_Ts for tumor were substantially higher than those of muscle and other background, suggesting specific binding of the tracer. Immunohistochemistry results confirmed the $\alpha_v\beta_3$ expression in tumor cells and neovasculature in squamous carcinoma patients. All these encouraging results indicate that PET with ^{18}F-alfatide prepared from a lyophilized kit can be applied to study $\alpha_v\beta_3$ expression during tumor progress and angiogenesis.

CONCLUSION

^{18}F-alfatide can be produced with excellent radiochemical yield and purity via a simple, 1-step lyophilized kit that can be ready for patient injection within 30 min. ^{18}F-alfatide PET allows specific imaging of $\alpha_v\beta_3$ expression in lung cancers with good contrast. This technique can be used for the assessment of angiogenesis and for planning and response evaluation of therapies that affect angiogenesis. More pilot studies of ^{18}F-alfatide in patients are required to further demonstrate the feasibility of antiangiogenic therapies combined with chemotherapy or radiotherapy in the future.

DISCLOSURE

The costs of publication of this article were defrayed in part by the payment of page charges. Therefore, and solely to indicate this fact, this article is hereby marked "advertisement" in accordance with 18 USC section 1734. This work was supported by the National Basic Research Program of China (973 program, 2013CB733802); the National Science Foundation of China (NSFC) (81028009, 81171399, 81101077, and 60972099); Jiangsu Province Social Development Program (BE2012622); Outstanding

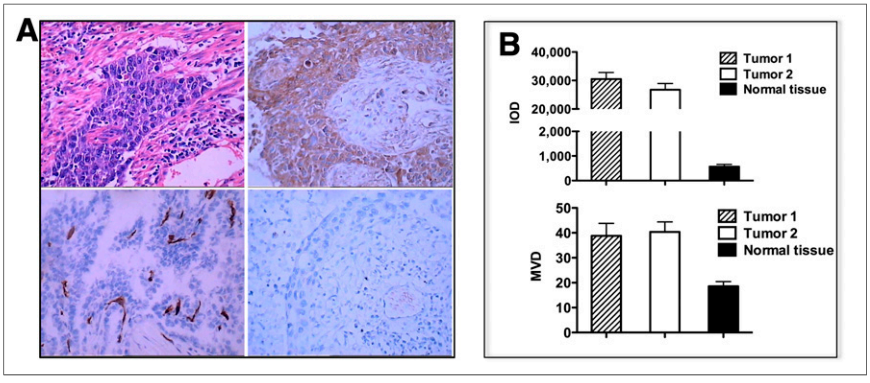

FIGURE 6. (A) Immunohistochemistry results: representative hematoxylin and eosin staining of tumor sample from lung cancer patient showing highly growing cancer cells spread to normal tissue (top left); immunohistochemistry with integrin antibody demonstrating $\alpha_v\beta_3$ expression predominantly on tumor cells (top right); immunohistochemistry staining of tumor vasculature with antibody against CD31 (bottom left); and immunohistochemistry staining of normal tissue, indicating rare expression of integrin $\alpha_v\beta_3$ (bottom right). (B) Quantification of integrin expression level in tumor tissue (upper) and microvessel density. IOD = integrated optical density; MVD = microvessel density.

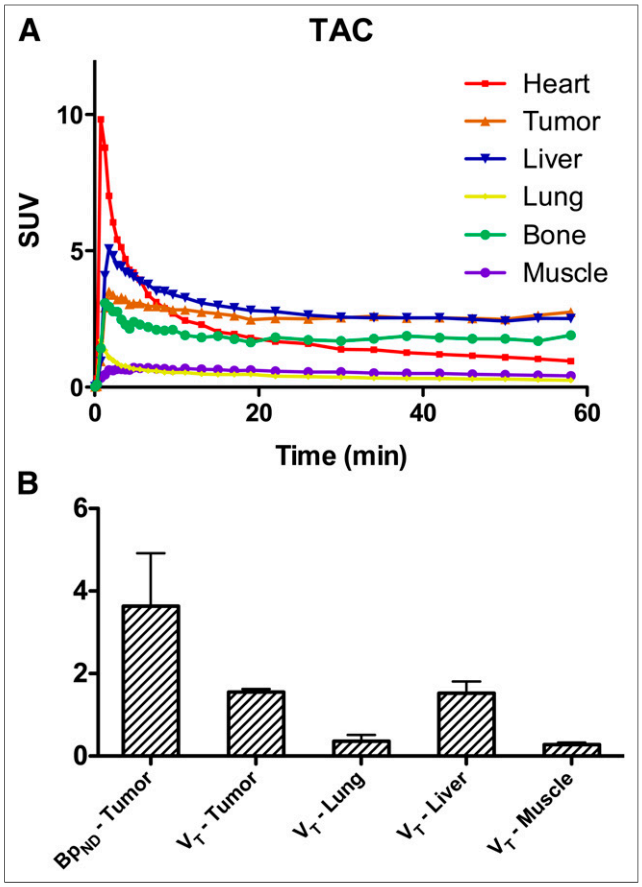

FIGURE 7. (A) Representative time–activity curves derived from 60-min dynamic PET scans. (B) Kinetic parameter quantifications Bp_{ND} and V_T for tumor and main organs. Bp_{ND} = binding potential; V_T = volume of distribution.

Professional Fund of Health Ministry in Jiangsu Province (RC2011095); Intramural Research Program of the National Institute of Biomedical Imaging and Bioengineering (NIBIB), National Institutes of Health (NIH); and China Scholarship Council (CSC). No other potential conflict of interest relevant to this article was reported.

REFERENCES

1. Singh M, Ferrara N. Modeling and predicting clinical efficacy for drugs targeting the tumor milieu. *Nat Biotechnol.* 2012;30:648–657.
2. Kubota Y. Tumor angiogenesis and anti-angiogenic therapy. *Keio J Med.* 2012;61:47–56.
3. Chauhan VP, Stylianopoulos T, Martin JD, et al. Normalization of tumour blood vessels improves the delivery of nanomedicines in a size-dependent manner. *Nat Nanotechnol.* 2012;7:383–388.
4. Beer AJ, Kessler H, Wester HJ, Schwaiger M. PET imaging of integrin $\alpha_v\beta_3$ Expression. *Theranostics.* 2011;1:48–57.
5. Haubner R, Wester HJ. Radiolabeled tracers for imaging of tumor angiogenesis and evaluation of anti-angiogenic therapies. *Curr Pharm Des.* 2004;10:1439–1455.
6. Mittra ES, Goris ML, Iagaru AH, et al. Pilot pharmacokinetic and dosimetric studies of ^{18}F-FPPRGD2: a PET radiopharmaceutical agent for imaging $\alpha_v\beta_3$ integrin levels. *Radiology.* 2011;260:182–191.
7. Hood JD, Cheresh DA. Role of integrins in cell invasion and migration. *Nat Rev Cancer.* 2002;2:91–100.
8. Brooks PC, Montgomery AM, Rosenfeld M, et al. Integrin $\alpha_v\beta_3$ antagonists promote tumor regression by inducing apoptosis of angiogenic blood vessels. *Cell.* 1994;79:1157–1164.
9. Niu G, Chen X. Why integrin as a primary target for imaging and therapy. *Theranostics.* 2011;1:30–47.
10. Zhou Y, Chakraborty S, Liu S. Radiolabeled cyclic RGD peptides as radiotracers for imaging tumors and thrombosis by SPECT. *Theranostics.* 2011;1:58–82.
11. Morrison M, Cuthbertson A. Integrin imaging to evaluate treatment response. *Theranostics.* 2011;1:149–153.
12. Liu S, Liu H, Ren G, Kimura RH, Cochran JR, Cheng Z. PET imaging of integrin positive tumors using ^{18}F labeled knottin peptides. *Theranostics.* 2011;1:403–412.
13. Lang L, Li W, Jia HM, et al. New methods for labeling RGD peptides with Bromine-76. *Theranostics.* 2011;1:341–353.
14. Chen X, Park R, Shahinian AH, et al. ^{18}F-labeled RGD peptide: initial evaluation for imaging brain tumor angiogenesis. *Nucl Med Biol.* 2004;31:179–189.
15. Chen X, Liu S, Hou Y, et al. MicroPET imaging of breast cancer $\alpha_v\beta_3$-integrin expression with ^{64}Cu-labeled dimeric RGD peptides. *Mol Imaging Biol.* 2004; 6:350–359.
16. Jeong JM, Hong MK, Chang YS, et al. Preparation of a promising angiogenesis PET imaging agent: ^{68}Ga-labeled c(RGDyK)-isothiocyanatobenzyl-1,4,7-triaza-cyclononane-1,4,7-triacetic acid and feasibility studies in mice. *J Nucl Med.* 2008;49:830–836.
17. Li ZB, Chen K, Chen X. ^{68}Ga-labeled multimeric RGD peptides for microPET imaging of integrin $\alpha_v\beta_3$ expression. *Eur J Nucl Med Mol Imaging.* 2008;35: 1100–1108.
18. Jacobson O, Zhu L, Niu G, et al. MicroPET imaging of integrin $\alpha_v\beta_3$ expressing tumors using ^{89}Zr-RGD peptides. *Mol Imaging Biol.* 2011;13:1224–1233.
19. Kenny LM, Coombes RC, Oulie I, et al. Phase I trial of the positron-emitting Arg-Gly-Asp (RGD) peptide radioligand ^{18}F-AH111585 in breast cancer patients. *J Nucl Med.* 2008;49:879–886.
20. Shi J, Zhou Y, Chakraborty S, et al. Evaluation of in-labeled cyclic RGD peptides: effects of peptide and linker multiplicity on their tumor uptake, excretion kinetics and metabolic stability. *Theranostics.* 2011;1:322–340.
21. Lang L, Li W, Guo N, et al. Comparison study of [^{18}F]FAl-NOTA-PRGD2, [^{18}F]FPPRGD2, and [^{68}Ga]Ga-NOTA-PRGD2 for PET imaging of U87MG tumors in mice. *Bioconjug Chem.* 2011;22:2415–2422.
22. Guo N, Lang L, Li W, et al. Quantitative analysis and comparison study of [^{18}F]AlF-NOTA-PRGD2, [^{18}F]FPPRGD2 and [^{68}Ga]Ga-NOTA-PRGD2 using a reference tissue model. *PLoS ONE.* 2012;7:e37506.
23. Guo N, Lang L, Gao H, et al. Quantitative analysis and parametric imaging of ^{18}F-Labeled monomeric and dimeric RGD peptides using compartment model. *Mol Imaging Biol.* 2012;6:743–752.
24. Logan J, Fowler JS, Volkow ND, et al. Graphical analysis of reversible radioligand binding from time-activity measurements applied to [N-^{11}C-methyl]-(-)-cocaine PET studies in human subjects. *J Cereb Blood Flow Metab.* 1990;10:740–747.
25. Kimura Y, Naganawa M, Shidahara M, Ikoma Y, Watabe H. PET kinetic analysis–pitfalls and a solution for the Logan plot. *Ann Nucl Med.* 2007;21:1–8.
26. Ferl GZ, Dumont RA, Hildebrandt IJ, et al. Derivation of a compartmental model for quantifying ^{64}Cu-DOTA-RGD kinetics in tumor-bearing mice. *J Nucl Med.* 2009;50:250–258.
27. Logan J, Fowler JS, Volkow ND, Wang GJ, Ding YS, Alexoff DL. Distribution volume ratios without blood sampling from graphical analysis of PET data. *J Cereb Blood Flow Metab.* 1996;16:834–840.
28. Liu S, Liu H, Jiang H, Xu Y, Zhang H, Cheng Z. One-step radiosynthesis of ^{18}F-AlF-NOTA-RGD2 for tumor angiogenesis PET imaging. *Eur J Nucl Med Mol Imaging.* 2011;38:1732–1741.
29. Chen X. Multimodality imaging of tumor integrin $\alpha_v\beta_3$ expression. *Mini Rev Med Chem.* 2006;6:227–234.
30. Battle MR, Goggi JL, Allen L, Barnett J, Morrison MS. Monitoring tumor response to antiangiogenic sunitinib therapy with ^{18}F-fluciclatide, an ^{18}F-labeled $\alpha_v\beta_3$-integrin and $\alpha_v\beta_5$-integrin imaging agent. *J Nucl Med.* 2011;52:424–430.
31. Chin FT, Shen B, Liu S, et al. First experience with clinical-grade [^{18}F]FPP (RGD)2: an automated multi-step radiosynthesis for clinical PET studies. *Mol Imaging Biol.* 2012;14:88–95.
32. Beer AJ, Grosu AL, Carlsen J, et al. [^{18}F]galacto-RGD positron emission tomography for imaging of $\alpha_v\beta_3$ expression on the neovasculature in patients with squamous cell carcinoma of the head and neck. *Clin Cancer Res.* 2007;13:6610–6616.
33. Zhu Z, Miao W, Li Q, et al. ^{99m}Tc-3PRGD2 for integrin receptor imaging of lung cancer: a multicenter study. *J Nucl Med.* 2012;53:716–722.